AD_____

Award Number: W81XWH-07-1-0228

TITLE: Developing a Zebrafish Model of NF1 for Structure-Function Analysis and Identification of Modifier Genes

PRINCIPAL INVESTIGATOR: Jonathan A. Epstein, M.D.

CONTRACTING ORGANIZATION: University of Pennsylvania
Philadelphia, PA 19104

REPORT DATE: April 2010

TYPE OF REPORT: Annual

PREPARED FOR: U.S. Army Medical Research and Materiel Command
Fort Detrick, Maryland 21702-5012

DISTRIBUTION STATEMENT:

X Approved for public release; distribution unlimited

REPORT DOCUMENTATION PAGE

Form Approved
OMB No. 0704-0188

1. REPORT DATE *(DD-MM-YYYY)*	2. REPORT TYPE	3. DATES COVERED *(From - To)*
01-04-2010	Annual	1 APR 2009 - 31 MAR 2010

4. TITLE AND SUBTITLE
Developing a Zebrafish Model of NF1 for Structure-Function Analysis and Identification of Modifier Genes

5a. CONTRACT NUMBER

5b. GRANT NUMBER
W81XWH-07-1-0228

5c. PROGRAM ELEMENT NUMBER

6. AUTHOR(S)
Jonathan A. Epstein, M.D.

5d. PROJECT NUMBER

5e. TASK NUMBER

5f. WORK UNIT NUMBER

7. PERFORMING ORGANIZATION NAME(S) AND ADDRESS(ES) AND ADDRESS(ES)
University of Pennsylvania
Philadelphia, PA 19104

8. PERFORMING ORGANIZATION REPORT NUMBER

9. SPONSORING / MONITORING AGENCY NAME(S) AND ADDRESS(ES)
U.S. Army Medical Research and Materiel Command
Fort Detrick, Maryland 21702-5012

10. SPONSOR/MONITOR'S ACRONYM(S)

11. SPONSOR/MONITOR'S REPORT NUMBER(S)

12. DISTRIBUTION / AVAILABILITY STATEMENT
Approved for Public Release; Distribution Unlimited

13. SUPPLEMENTARY NOTES

14. ABSTRACT No abstract provided.

15. SUBJECT TERMS **No subject terms provided.**

16. SECURITY CLASSIFICATION OF:			17. LIMITATION OF ABSTRACT	18. NUMBER OF PAGES	19a. NAME OF RESPONSIBLE PERSON
a. REPORT	b. ABSTRACT	c. THIS PAGE			USAMRMC
U	U	U	UU	27	19b. TELEPHONE NUMBER *(include area code)*

Table of Contents

Page

Introduction:

The primary goal of this project is to develop a zebrafish model of the autosomal dominant genetic disorder type I neurofibromatosis (NF1). This disorder is very common, affecting approximately 1 in 3000 live births, and results from mutations in the *NF1* gene. A zebrafish model of this disease will be particularly useful in furthering our understanding of the pathophysiology of this disorder and will allow the application of high throughput strategies to screen libraries of chemical compounds to identify small molecules that may prove efficacious in modulating NF1-associated phenotypes. The zebrafish model will also allow for rapid and cost-effective structure-function analysis of neurofibromin, the large protein product of the *NF1* gene. Zebrafish develop rapidly and are transparent throughout early development allowing for the easy visualization of many developing tissues, including the cardiovascular and nervous systems. In addition, the availability of transgenic reporter lines that express fluorescent proteins under the control of tissue-specific promoters allows for real-time visualization of complex developmental processes. This model system is also tenable to forward genetic screens, which will allow for the identification of enhancers and suppressors of NF1 phenotypes in an unbiased fashion. Prior to the efforts funded by this award, the zebrafish orthologues of the human *NF1* gene had not been described or characterized. This project involves the collaboration of two established groups to coordinate efforts in developing and exploiting a zebrafish model of this important genetic disease.

Body of work:

The coordinated efforts of the Look and Epstein laboratories have led to significant inroads into the primary objectives of this award. We outline below our collective progress since inception of this work reiterating aspects of our investigations described in our last annual report that have been significantly expanded upon along with new information not previously presented.

Identification of *nf1a* and *nf1b*

We utilized a bioinformatics approach to identify the zebrafish orthologues of human *NF1*. Analysis of the eighth assembly (Zv8) of the zebrafish genome revealed two genes highly similar to *NF1* at the amino acid level (90.4% and 90.7% respectively), which we named *nf1a* and *nf1b*. These genes are highly related to one another (87.4% identical and 93.7% similar) with *nf1a* and *nf1b* sharing similar genomic structures and each containing 57 exons (Fig 1A-B). *nf1a* is located on chromosome 15 (Fig 1A) and predicts a 311 kD protein composed of 2755 amino acids while *nf1b* is located on chromosome 10 (Fig 1B) and predicts a 310 kD protein composed of 2747 amino acids.

Comparison to Drosophila, murine, and human neurofibromin protein sequences reveals significant conservation in the GAP and IRA homology domains and also in extensive areas flanking these regions, suggesting additional functional motifs that have been conserved across evolution (Fig 2). A phylogenetic tree (Fig 1C) demonstrates a tight clustering of the zebrafish neurofibromin orthologues with other mammalian neurofibromins and a divergence from the Drosophila neurofibromin orthologue. Human/zebrafish synteny maps and bioinformatics analyses suggest that *nf1a* and *nf1b* likely arose via gene duplication (Fig 1D). Upstream of the human NF1 gene on chromosome 17 are genes encoding WD repeat and SOCS box-containing 1 (WSB1), Kinase suppressor of Ras 1 (KSR1), and Galectin-9 (LGALS9) while A kinase anchor protein 1 (AKAP1) and RNA-binding protein Musashi homolog 2 (MSI2) both lie downstream of NF1. Similar genes flank *nf1a*, while *nf1b* is flanked only by orthologues

of KSR1 and MSI2. The identification of duplicated genes is common in zebrafish and reflects the well-described chromosomal doubling event occurring early in teleost evolution.

***nf1a* and *nf1b* are expressed maternally and in the developing zebrafish cardiovascular system.**

The GenBank EST database identified expressed sequence tags for both zebrafish *nf1* genes in many tissues including the heart (Fig 4A) suggesting that neither gene is likely to be a pseudogene and that they are expressed in overlapping tissues. We examined the expression of both genes by whole mount *in situ* hybridization between the 4-cell stage and 4 days post fertilization (dpf) and found that both genes are expressed ubiquitously during early development with later restriction to regions of the head and anterior central nervous system (Fig 3A1-7, B1-7, Fig S2C1-C7, D1-D7). Notably, at 48 hours post fertilization (hpf) and 3 dpf both genes are expressed in the heart (Fig 3A4, B4, A6, B6, Fig 4C5-6, D5-6) and in the dorsal vessel (Fig 3A3, B3, A5, B5, Fig 4C7, D7). Reverse transcription and polymerase chain reaction (RT-PCR) using RNA from wild type 24, 72, and 84 hpf whole embryos or 3 dpf Tg(kdrl:GRCFP)zn1 GFP-positive sorted cells confirmed expression, particularly in the vascular endothelium (Figure 4E-G), while RNA from 1-cell embryos indicate that both genes are expressed maternally (Fig 4B). Queries of an expression database generated from sorted endothelial cells from Tg(fli1:egfp)y1 zebrafish identifies *nf1a* and *nf1b* in both GFP+ and GFP- cell populations, consistent with the expression of these genes in vascular endothelium.

Morpholino knockdown of nf1a and nf1b results in cardiovascular defects

nf1a and *nf1b* morphant embryos displayed gross abnormalities of cardiovascular development appreciable to the blinded observer by 48 hpf. Frequently, blood was seen to move back and forth from atrium to ventricle in morphants, suggesting a malfunctioning atrio-ventricular valve. At the resolution afforded to us by histological analysis, we observed no readily apparent structural defects in the atrio-ventricular valves of morphants despite the observed functional deficits (Fig 5). In addition, we observed pooling of blood in the common cardinal vein and a paucity of blood flow along the dorsal aorta and posterior cardinal vein. Valvular insufficiency and reduced blood flow were not seen in control morphants or wild type embryos. Overall development of the embryos was relatively preserved through the first 3 days despite these cardiac defects. Histological analysis revealed a thinned ventricular myocardium and large pericardial effusions in MO-treated embryos (Fig 6K-L, Fig 7A-B, F-G). Immunohistochemical analysis of 3.5 dpf *nf1a*, *nf1b*, and *nf1a/nf1b* morphant zebrafish also reveals increases in phospho-Erk staining (Fig 6M-N, Fig 7C-E, H-K). Gross morphological analysis showed an increased incidence of pericardial effusions beginning at 48 hpf, reflecting cardiac dysfunction, in *nf1a* and *nf1b* morhpants when compared with controls (Fig 6A-G, Fig 7L-M). Non-specific toxicity arising from MO exposure as a cause of the observed cardiovascular defects was unlikely as unrelated control or scrambled MOs failed to produce similar levels of abnormalities, defects were observed even at low doses of specific MOs, and similar defects were observed with several unrelated but specific MOs directed against *nf1a* and *nf1b*. In addition, injection of specific MOs in *p53* mutant embryos also produced similar cardiovascular defects (Fig 6H-J), and off-target effects due to MO exposure are known to be partially mediated through *p53* activation. Defects in cardiac valve morphogenesis and a thinning of the ventricular myocardium are also seen in *Nf1*$^{-/-}$ murine embryos.

We performed knockdown experiments using zebrafish embryos in which endothelial cells are marked by expression of a cytoplasmic enhanced green fluorescent protein (GFP) in order to allow for a more detailed analysis of vascular development. Dramatic abnormalities of vascular patterning in the intersomitic vessels of morphant embryos were seen at 48 and 72 hpf (Fig 8). In *nf1a* MO-treated embryos, the leading edge of the sprouting vessels displayed claw-like projections at 48 hpf (Fig 8C)

and failed to pattern normally such that the dorsal longitudinal anastomotic vessel (DLAV) did not form or developed in a rudimentary fashion (Fig 8F). This occurred in embryos that were otherwise normal in overall size and maturity. These defects were also noted in *nf1a/nf1b* compound morphants, and were present but less severe in *nf1b* morphants. Vascular patterning defects did not appear to correlate directly with cardiac defects, as we observed embryos with vascular abnormalities that did not display pericardial effusion or valvular insufficiency as assessed by a "to-and-fro" movement of blood within the heart. Blood flow within the dorsal aorta and posterior cardinal vein appeared intact in these embryos.

At 24 hpf, analysis using zebrafish embryos expressing a nuclear-localized GFP in endothelial cells indicated that morphants displayed a complete (Fig 9A4) or partial absence of intersomitic vessels emanating from the dorsal aorta when compared with stage-matched controls (Fig 9A3). Overall morphology of morphant and control embryos appeared equivalent (Fig 9A1-2) ruling out non-specific developmental delay. These defects were apparent following MO-mediated knockdown of *nf1a* or *nf1b* while knockdown of both together had an additive effect (Fig 9B). The small percentage of embryos with defects produced by the 5MP MO may have been due to low-level knockdown of *nf1a*. Again, similar defects were observed with several unrelated but specific MOs directed against *nf1a* and *nf1b* (Fig 10A). Our analysis of morphant embryos at 24 hpf also revealed a caudal vessel defect. Morphant embryos displayed a cystic expansion in the region of the caudal vein and exhibited inappropriate anastomoses between the caudal vein and artery (Fig 10D2-D4) when compared with controls (Fig 10D1). Identity of the expanded tissue as vascular was confirmed by expression of GFP (Fig 10D6-ZFN_MUT2) and the observation of a pooling of red blood cells in the expanded region. This defect was present following knockdown of *nf1a*, *nf1b*, or both together (Fig 10C-D).

Additional confirmation of the role of *nf1a*/*nf1b* in vascular development derives from studies using a genetic background sensitized to vascular insult. Previous studies employed MOs directed against *flt4*, the zebrafish VEGF receptor-3 orthologue, to investigate genetic interactions during zebrafish artery development. Additionally, *flt4* morphant zebrafish embryos display variable defects in segmental artery formation reminiscent of those identified in our *nf1a/nf1b* morphants. Endothelial-GFP expressing zebrafish embryos were injected with *flt4* MO alone and in combination with a MO directed against *nf1a*, *nf1b*, or a combination of both. At low MO doses, 85% of *flt4*/*nf1a*, 24% of *flt4*/*nf1b*, and 36% of *flt4/nf1a + nf1b* compound morphants, displayed abnormal vascular shunts at 48 hpf compared to only 3-8% of individual *flt4*, *nf1a*, or *nf1b* morphants (Fig 9C, Fig 10B). This defect was not apparent in control morphants. The shunts occur between the dorsal aorta and the dorsal longitudinal anastomotic vessel with retrograde flow through segmental arteries back into the dorsal aorta or through intersegmental veins into the posterior cardinal vein. In some cases, there were interruptions of the dorsal aorta.

***nf1* loss promotes OPC migration.**

We have shown previously that oligodendrocyte precursor cell (OPC) numbers are increased upon transient *nf1* knockdown by morpholino. Here we report our analysis of the behavior of OPCs following *nf1* knockdown by performing live time-lapse imaging of these cells *in vivo.* The *olig2-EGFP* transgenic animals were monitored for 12 hours, beginning at 60 hpf when OPCs start to actively migrate away from the ventral spinal cord. Compared to, control *p53 e7/e7* animals, more OPCs migrated into the dorsal spinal cord in *nf1a+1b*-knockdown *p53 e7/e7* embryos (Fig 11A, B), consistent with our observations from fixed sections (see our 2009 progress report). Interestingly, the time-lapse study also revealed that *nf1a+1b*-morphant OPCs traveled longer distances relative to control animals (Fig 11E). When representative migratory traces of individual OPC cells were analyzed from the time-

lapse movies, *nf1a+1b*-knockdown OPCs were found to migrate further in the dorsal and rostro-caudal directions than control OPCs (Fig 11C and D). Analysis of individual OPC cell movements over the 12-hour imaging period showed a 35% increase in the total distance traveled by the progenitors in *nf1* knockdown animals (32.05 μm in control vs. 43.27 μm in *nf1a+1b*-morphant, $p<0.05$; n=9 and n=23, respectively; Fig 11E). In all cases the OPCs display intermittent movement consisting of repeated cycles of active migration, separated by stationary pauses that often distinguish new trajectories from the preceding path. After *nf1* knockdown, the OPCs paused for shorter periods of time relative to controls (413.9 min in control vs. 324.3 min in *nf1a+1b*-morphant; $p<0.005$; Fig 11F), however, the frequency of the pauses did not differ significantly (2.28/hr in control vs. 2.58/hr in *nf1a+1b*-morphant; $p>0.1$). Furthermore, the velocities of OPCs during active migration were determined and found to be unaffected *by nf1* knockdown (0.5203 μm/5min in control vs. 0.5343 μm/5min in *nf1a+1b*-morphant; $p>0.7$; Fig 11G). Taken together, these findings demonstrate a novel *in vivo* phenotype of OPCs in *nf1a+1b*-morphants where they spend more time actively migrating as a result of decreases in their period of inactivity.

The increase of OPC number upon *nf1* knockdown depends on the GAP activity of NF1

The best-known function of human NF1 is to act as a RAS-GTPase-activating protein (GAP) to downregulate RAS signaling. To investigate whether the increase in OPCs seen in our model depends upon the GAP activity of NF1, we performed rescue experiments, injecting mRNA encoding the GRD of human NF1 into *nf1a+1b*-knockdown embryos at the one-cell stage. To confirm and monitor GRD expression, we fused the coding sequence of the *GRD* domain in-frame with the gene encoding mCherryRed fluorescent protein at its N terminus. The *nf1a+1b*-knockdown embryos coinjected with *mCherryRed* RNA as a control showed the expected increase in OPC numbers relative to control MO- and control RNA-injected embryos (Fig 12B-D). *nf1a+1b*-knockdown embryos coinjected with the *GRD* RNA showed a relative reduction in the number of OPCs in the dorsal spinal cord from 67.7/embryo to 48.5/embryo (n=10, $p<0.001$; Fig 12A, B, E). Furthermore, the number of OPCs present in *nf1a+1b*-knockdown embryos as a result of *GRD* rescue did not differ significantly from the numbers of OPCs present in control MO- and control RNA-injected embryos (48.5 vs. 47.5, $p>0.7$, and 48.5 vs. 57.5, $P>0.1$, respectively). These results indicate that the increase in OPC numbers due to *nf1* deficiency is mediated by the loss of GAP activity.

Generating zebrafish *nf1a* and *nf1b* mutants by TILLING

An important aspect of our proposal requires the generation of stable zebrafish lines harboring mutations in *nf1a* and *nf1b*. We will use these animals to verify the data we collected from our morpholino studies as well as to extend our analysis to time points beyond those accessible using transient knockdown assays. In order to generate stable zebrafish lines carrying mutations in *nf1a* and *nf1b* we have used a reverse genetics approach called TILLING (Target Induced Local Lesions In Genomes), in collaboration with the laboratory of Dr. Solnica-Krezel, and have found several *nf1a* missense mutant alleles and one nonsense mutant line in the *nf1a* gene (Fig 13A-B). A second mutagenesis strategy based on retroviral insertion identified a single mutant line affecting the *nf1b* locus in the intron between exon 1 and 2 (Fig 13B). These mutants will be tested for potential defects in oligodendrocyte and cardiovascular development, along with the mutant lines from a reverse genetics approach using zinc-finger nucleases, discussed below.

Zinc Finger Nuclease (ZFN)-induced *nf1a* and *nf1b* mutant alleles

As previously outlined in our proposal, the generation of stable *nf1a* and *nf1b* mutant zebrafish lines remains a necessary prerequisite to performing the large scale chemical and genetic screens we argue will be invaluable to furthering our understanding of NF1 biology and lead to the development of novel therapeutic agents. While we encountered some success in generating *nf1a* mutant lines using the TILLING approach, this method lacked the efficiency necessary to generate multiple loss-of-function mutant alleles. Therefore, we turned to emerging technologies that promised a more efficient rate of specific lesion-induction in the zebrafish genome.

Excitingly, a cutting-edge strategy for targeted mutagenesis was developed for zebrafish using zinc finger nuclease (ZFN) technology. We were fortunate to have the opportunity to collaborate closely with the laboratories of Nathan Lawson and Scot Wolfe to apply this technology to generate stable mutant *nf1a* and *nf1b* zebrafish lines. Briefly, we utilized a modular approach to generate two zinc finger proteins, each with a 9-bp sequence specific recognition element. Each of these proteins is coupled to a monomer of the heterodimeric FokI restriction endonuclease. *In vitro* synthesized RNA encoding these ZFNs are injected into 1-cell zebrafish embryos where they are translated into protein and bind to there cognate target sequences in the zebrafish genome within exons of *nf1a* and *nf1b*. This binding occurs such that the two FokI restriction endonuclease monomers are brought into close proximity of each other allowing them to form a functional dimer and introduce a double-stranded break in the DNA. These double-stranded breaks are repaired by the error-prone non-homolgous end-joining (NHEJ) pathway leading to microinsertions and microdeletions at the site of the double-stranded break. The Look and Epstein laboratories have collaboratively generated multiple ZFNs directed against *nf1a* (exon 25) and *nf1b* (exon 19). This combined effort has led to the generation 7 different *nf1a* and *nf1b* mutant alleles all harboring frame shifts that result in premature stop codons (Figure 14). As the GAP-related domain in *nf1a* and *nf1b* span exon 26 and exon 27, we expect that these frame-shift mutations within exon 25 of *nf1a* and exon 19 of *nf1b* should result in proteins that lack functional GAP activity.

Redundant function of the *nf1a* and *nf1b* alleles

We generated single homozygous mutant alleles of *nf1a* and *nf1b*, however they failed to show any significant abnormalities from embryogenesis through adulthood. However, when *nf1b*-specific morpholinos were injected into $nf1a^{ZFN\_mut2/\ ZFN\_mut2}$ mutant embryos, an increased OPC phenotype, similar to *nf1a* and *nf1b* double morphants, was observed (data not shown). This result suggests that $nf1a^{ZFN\_mut2}$ has no functional nf1a protein and that nf1b shares redundant function with nf1a.

Due to the lack of a mutant phenotype *nf1a* and *nf1b* single homozygous mutants, we generated *nf1a;nf1b* double mutants. We crossed two ZFN-induced nf1a mutant alleles and the *nf1a*-nonsense tilling mutant with two mutant alleles of *nf1b* ($nf1a^{ZFN\_mut2};nf1b^{ZFN\_mut2}$, $nf1a^{ZFN\_mut1};nf1b^{ZFN\_mut3}$ and $nf1a^{T203};nf1b^{ZFN\_mut2}$). To analyze tissue-specific phenotypes we intercrossed 6 different transgenic lines with the *nf1a;nf1b* double mutants (see Table 2) to ascertain cell type-specific phenotypes in the CNS and PNS. We also found that *nf1a;nf1b* double homozygous mutants start to die around 7 dpf and that the majorty fail to survive beyond 9 to 10 dpf. The double mutants exhibit severe brain degeneration that may be a primary cause of lethality. All three combinations of *nf1a;nf1b* double mutant alleles exhibited the identical phenotype supporting the redundant roles of nf1a and nf1b and that they are essential for survival as in mammals.

Hyperplastic OPCs and SCG in the *nf1a;nf1b* double mutant

Although *nf1a;nf1b* double homozygous mutant larvae do not survive beyond 10 dpf, their general morphology appears relatively normal until 7 or 8 dpf (see Fig. 15B of confirmed mutant genotypes). Most double mutant larvae lacked melanocytes in the lateral stripe, which could first be

detected at 4 dpf and persisted until death (Fig. 15C and 15D). Furthermore, the double mutant larvae exhibited increased yellow pigmentation, indicative of altered xanthophore development and may correlate with increased café-au-lait spots often seen in human NF1 patients. We have now confirmed that we can use this phenotype to identify double mutant animals prior to PCR genotyping, which simplifies our experimental protocols immensely.

Because *nf1a* and *nf1b* double morphants have excess OPCs in the spinal cord, we promptly confirmed this phenotype in *Tg(olig4:egfp);nf1a*$^{ZFN\_mut2/ZFN\_mut2}$*;nf1b*$^{ZFN\_mut2/ZFN\_mut2}$ mutants and found that they had more dorsally migrated OPCs in the spinal cord than wild-type control animals at 6 dpf (Fig. 4E and 4F). Increased numbers of OPCs could be detected as early as 3 dpf in the double mutants, which persisted up to their death (data not shown). This result is consistent with our morphant data and the mouse Nf1-loss phenotype.

The earliest report of *Nf1* knockout mice demonstrated the *Nf1* homozygous mutant had hyperplasia in the neurons of sympathetic ganglion tissue. To check whether zebrafish *nf1a* and *nf1b*-loss induces a similar defect, we examined superior cervical sympathetic ganglion (SCG) tissue by crossing the mutant to the *Tg(dbh:gfp)* transgenic line. As shown in Fig 15G and 15H, the *nf1a*$^{ZFN\_mut2/ZFN\_mut2}$*;nf1b*$^{ZFN\_mut2/ZFN\_mut2}$ mutant has an enlarged SCG relative to wild type animals, indicating that the function of *nf1* genes in zebrafish is conserved with Nf1 function in mice.

In order to address whether Ras signaling is activated in the double mutant, we performed immunohistochemistry using phospho-ERK 1/4 antibody. At 5 dpf, a few neurons in the spinal cord of wild-type larvae express pERK1/4 strongly, while most other cells express it weakly (Fig. 15I). However, in the double mutant, in addition to a subset of neurons, the white matter of neurons in the spinal cord are show strong expression, indicating that ERK signaling is highly active in the axons of neurons in the mutant (Fig. 15J). Furthermore, the basal level of ERK1/4 phosphorylation appears relatively higher in most tissues (Fig. 15J). These findings suggest that *nf1a* and *nf1b* loss leads to activation of the ERK pathway, which is one of the main downstream signaling of Ras pathway.

In summary

• Transient loss-of-function of *nf1a* and *nf1b* in zebrafish yields a range of cardiac, vascular, and neural phenotypes that we have carefully defined and characterized.
• Several stable lines of zebrafish harboring loss-of-function alleles for *nf1a* and *nf1b* have been identified and validated

Materials and Methods

1. OPC Imaging and statistical analyses. For time-lapse movies, a Zeiss 200M inverted microscope equipped with a spinning-disc confocal system (Yokogawa) was used. The statistical significance of changes to OPC cell numbers and migration upon nf1 knockdown was determined by t-test analysis.

2. GRD rescue. The construct for containing the mCherryRed-GRD fusion protein was first created using the multisite Gateway system (InVitrogen) and subcloned into the pCS2+ vector in order to synthesize sense RNA in vitro. Sense RNA for the mCherryRed fluorescent protein was synthesized and served as an injection control. Approximately 15 pg of mCherryRed-GRD RNA or 6 pg of mCherryRed were injected for the rescue experiments, along with appropriate morpholinos.

3. *In situ* hybridization. *nf1a* (ENSDARG00000012982) and *nf1b* (ENSDARG00000004184) predicted cDNA sequences from Ensembl (http://www.ensembl.org/) were subjected to VISTA analysis (http://genome.lbl.gov/vista/) and the two regions of greatest dissimilarity were PCR amplified for both

genes (*nf1a* from bp 865-1518: 5′-GGGGGAGAGGAGAAAGCTAA and 5′-GGGGTCAGCGTGGATAAGT; *nf1a* from bp 6638 to 7236: 5′-CCACAGTCATCGCTCTCACC and 5′-GGCTACTGCGTGAAAACCAG; *nf1b* from bp 770 to1491: 5′-CCGAAAGCACGAAGAGAAAA and 5′-TCTGCTCTTGGCTCTGGTG; *nf1b* from bp 6798 to 7320: 5′-CGAGGAGGTGTTTATGGAGA and 5′-GGTGTTGACTTGAGAGGGTTG) from 24 hpf pooled zebrafish cDNA and cloned into the pCRII-TOPO vector (Invitrogen). *GFAP in situ* probe was PCR amplified from zebrafish 3dpf pooled cDNA (5′- AGCGTTCCTTCTCATCCTACCGAA and 5′-GCAGTCTCGTCTTGAAGTCTCTGT) and cloned into the pCRII-TOPO vector (Invitrogen). Antisense RNA probes for *nf1a* and *nf1b* (from bp 6798-7320) were generated by linearization with EcoRV digestion, followed by transcription with SP6 polymerase. An antisense RNA probe for *nf1b* (from bp 770 to 1491) was generated by linearization with NotI digestion, followed by transcription with SP6 polymerase. Processed embryos were mounted in 100% glycerol and photographed.

4. Western blotting. Whole zebrafish 3.5 dpf protein lysates (50-100μg) were separated by gel electrophoresis, transferred to PVDF membranes (Invitrogen) and probed overnight at 4ºC with the following primary antibodies: anti-neurofibromin (Abcam Ab17963, 1:1000), anti-phospho-p44/42 MAPK (Cell Signaling 7100, 1:100; Cell Signaling 4377, 1:1000), anti-p44/42 MAPK (Cell Signaling 9102, 1:1000), and anti-alpha-tubulin (Sigma T6074, 1:1000). Primary antibody binding was visualized using the Western Breeze Immunodetection Kit (Invitrogen) according to manufacturer instructions.

5. Imaging and statistical analysis. Developing Tg(fli1:egfp)y1,Tg(fli:negfp)y7, and Tg(kdr:GRCFP)zn1 zebrafish embryos were mounted in low-melt agarose supplemented with tricaine methanesulfonate (MS-222) and imaged using a Leica TCS SPII confocal laser scanning microscope. Single vertical projections of three-dimensional datasets (60 optical sections at 2μm intervals from a 10X water immersion lens) were generated as TIFF images using the Leica Confocal Software package (Leica). Transmitted light images were captures using an Olympus MVX10 microscope and Olympus DP72 digital camera (Olympus). The SAS/STAT software package (SAS) was used to perform statistical analyses for ordinal data using a Mann-Whitney U test while continuous data was analyzed using a Student′s t-test.

6. Histology. Briefly, samples were washed with ice-cold PBS, fixed overnight in 4% paraformaldehyde, washed with PBS, and dehydrated through an ethanol series prior to paraffin embedding. Anti-phospho-p44/42 MAPK antibody (Cell Signaling 4370) was used at manufacturer suggested concentration.

7. Flow Cytometry and Quantitative PCR. Fluorescence activated cell sorting (FACS) was performed on whole single cell suspensions generated from 3.5 dpf wild type and Tg(kdrl:GRCFP)zn1 zebrafish embryos. Briefly, embryos were rinsed in calcium free Ringer's solution (116 mM NaCl, 2.9 mM KCl, 5 mM HEPES [pH=7.2]), deyolked, and incubated in protease solution (0.25% trypsin, 1 mM EDTA; in PBS [pH=8]) at 28 degrees Celsius with intermittent agitation by repeated pipetting through a 200 uL tip. Upon generation of a single cell suspension, reaction was stopped by addition of 10% fetal calf serum. Cells were rinsed in suspension solution (Leibovitz L-15 Medium, 0.8 mM CaCl2, Penicillin [50 U/mL], Streptomycin [0.05 mg/ml], 1% fetal calf serum), filtered successively through 100 μm and 40 μm cell strainers, and sorted using a BD FACSAria cell sorter into collection medium (Leibovitz L-15 Medium, 0.8 mM CaCl2, Penicillin [50 U/mL], Streptomycin [0.05 mg/ml], 10% fetal calf serum). Quantitative PCR was performed for *cdh5* (5′-AAATGGCACAGACCTCTTCA and 5′-CTCACGGTCGAGGTCACTT), *etsrp* (5′-ACTCCTGCTGGATTCTGCTT and 5′-GGCCACGACTGAGCTTCT), and *ef1a* (5′-CTTCGTCCCAATTTCAGGAT and 5′-GAACCAGCCCATGTTTGAG).

Key research accomplishments:

- Characterization of zebrafish orthologs: *nf1a* and *nf1b*.
- *Further Analysis of gene expression of nf1a and nf1b.*
- *Further analysis of morpholino knockdown phenotypes for nf1a and nf1b.*
- *Generation of zebrafish lines harboring mutations in nf1a and nf1b via TILLING and through the use of engineered Zinc Finger Nucleases.*
- *Initial phenotypic analysis of nf1a/nf1b double homozygous mutant zebrafish embryos*.

Reportable outcomes:
A manuscript reporting our cardiovascular findings following MO-mediated transient loss-of-function of *nf1a* and *nf1b* was published in *PNAS*.

Cardiac and vascular functions of the zebrafish orthologues of the type I neurofibromatosis gene NFI. Padmanabhan A*, Lee JS*, Ismat FA, Lu MM, Lawson ND, Kanki JP, Look AT^, Epstein JA^. Proc Natl Acad Sci U S A. 2009 Dec 29;106(52):22305-10. Epub 2009 Dec 4.

* = These authors contributed equally to this work
^ = Corresponding authors

A second manuscript reporting our neural findings following MO-mediated transient loss-of-function of *nf1a* and *nf1b* is presently in the review process at *Human Molecular Genetics*. In addition, multiple abstracts and oral presentations stemming from this work have been presented at various meetings including the University of Pennsylvania Cardiovascular Institute Symposium, University of Pennsylvania Cell and Molecular Biology Symposium, The 6th European Zebrafish Development and Genetics Meeting, and The Mid-Atlantic Regional Zebrafish Meeting.

Conclusion:
In this third year of study, we have significantly furthered our advances towards meeting the goals set forth in the funded proposal. The target genes have been clearly identified and phenotypes due to morpholino knockdown have been characterized that are relevant to the understanding of human disease. Our efforts towards this end have resulted in a published manuscript with a second presently in the review process. While morpholino knockdown is informative, future experiments will be aided by the characterization of stable mutations within these genes in zebrafish. We have now obtained these mutant fish lines using several different approaches. When characterized, these reagents will be freely shared with our colleagues. These reagents should be excellent candidates for use in screening small molecules and for use in performing genetic screens to identify modulators of this important disease.

Supporting Data:

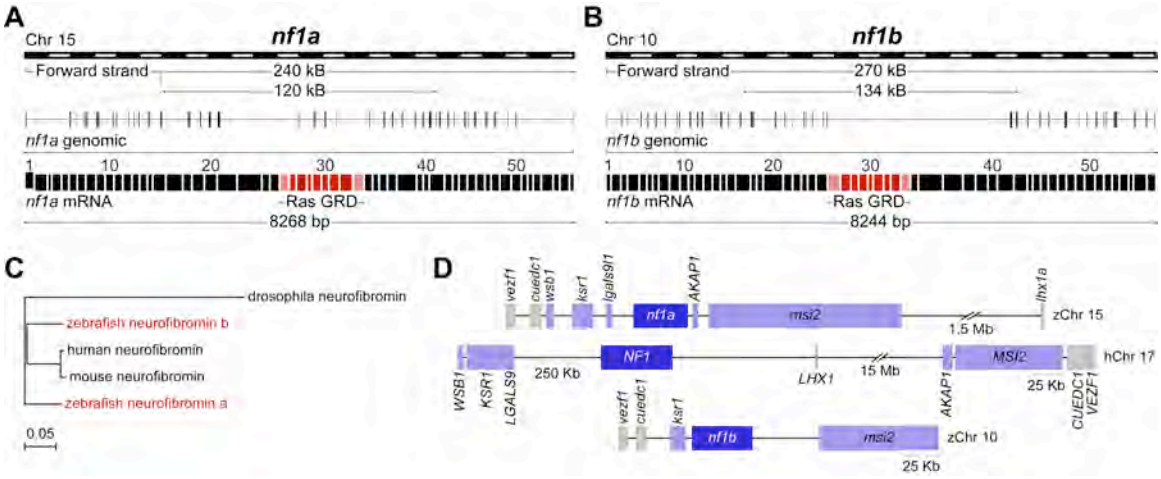

Fig 1. **Zebrafish have two orthologues of human *NF1*.**
(**A**, **B**) Genomic and mRNA structures of the two orthologous zebrafish genes corresponding to human *NF1*. (**C**) Phylogenetic tree comparison of zebrafish, human, mouse, and Drosophila neurofibromin. (**D**) Analysis of syntenic relationships between human chromosome 17 (*NF1)* and zebrafish chromosomes 15 (*nf1a*) and 10 (*nf1b*). Relative genomic positions are to scale as indicated.

Fig 2. Zebrafish *NF1* orthologues are highly conserved within the GAP-related domain. Amino acid sequence alignment reveals a remarkably high degree of protein conservation within the human, mouse, zebrafish, and drosophila neurofibromin GAP-related domains (identical amino acid highlighted grey, similar amino acids highlighted yellow, and mismatched amino acids not highlighted). Alternatively spliced exon 23a in human *NF1* (not depicted) is present in both *nf1a* and *nf1b*.

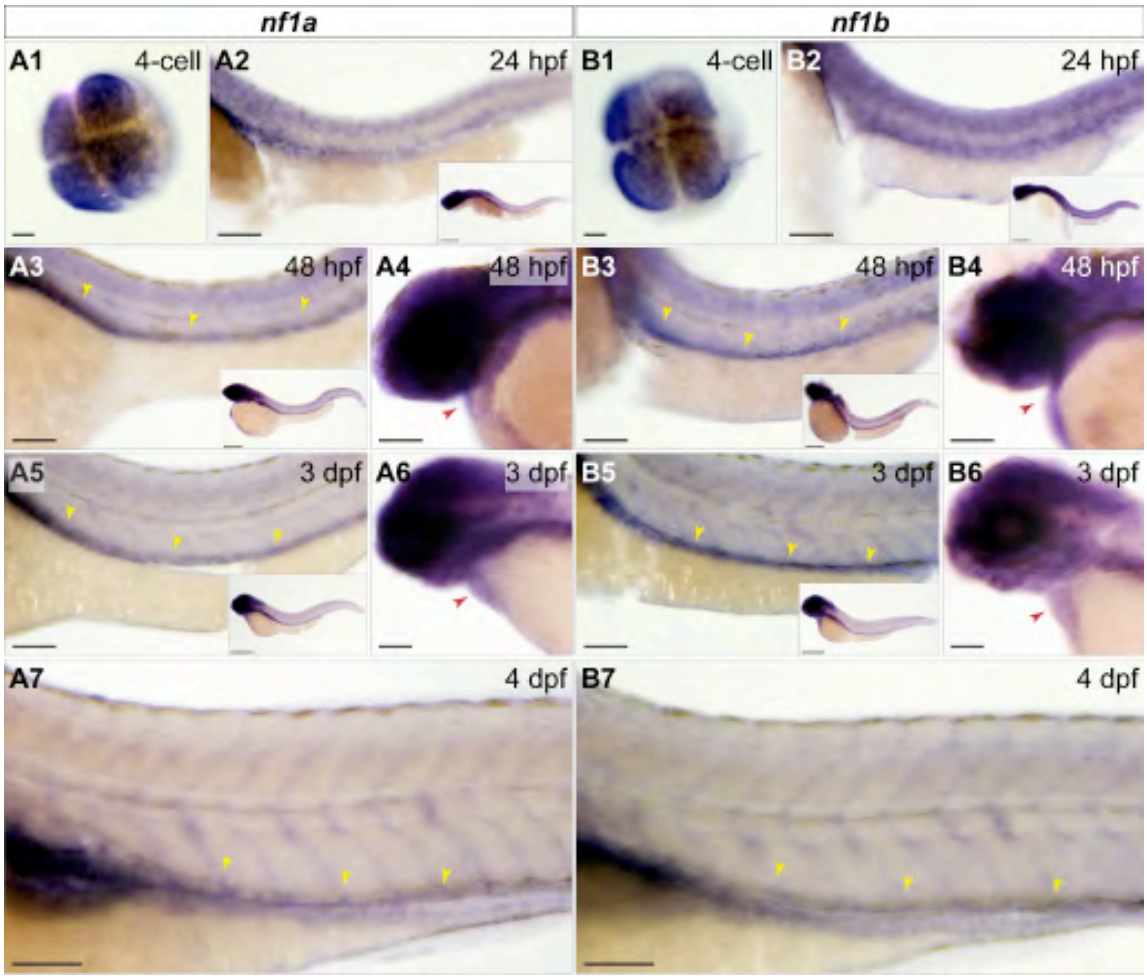

Fig 3. ***nf1a* and *nf1b* are expressed maternally and in the developing zebrafish cardiovascular system.**

Whole-mount *in situ* hybridization for *nf1a* and *nf1b* at the 4-cell stage, 24 hpf, 48 hpf, 3dpf, and 4 dpf. (**A1, B1**) At the 4-cell stage, *nf1a* and *nf1b* are expressed throughout the animal pole of the developing embryo. (**A2, B2**) Both genes are expressed broadly at 24 hpf (inset), with strong expression along the spinal cord. (**A3, B3**) At 48 hpf, expression of *nf1a* and *nf1b* is noted in the head and regions of the anterior trunk (inset). Spinal cord expression of both genes persists and positive staining is observed along the dorsal vessel for *nf1a* and *nf1b*. (**A4, B4**) Cardiac expression for both genes is observed at 48 hpf. (**A5, B5**) Expression of *nf1a* and *nf1b* become progressively restricted to regions of the head at 3 dpf (insets). *nf1a* and *nf1b* expression along the dorsal vessel (**A5, B5**) and in the embryonic heart (**A6, B6**) persist at 3 dpf. (**A7, B7**). At 4 dpf, robust vascular staining is apparent for *nf1a* and *nf1b*. Scale bars: 25μm (100μm for insets).

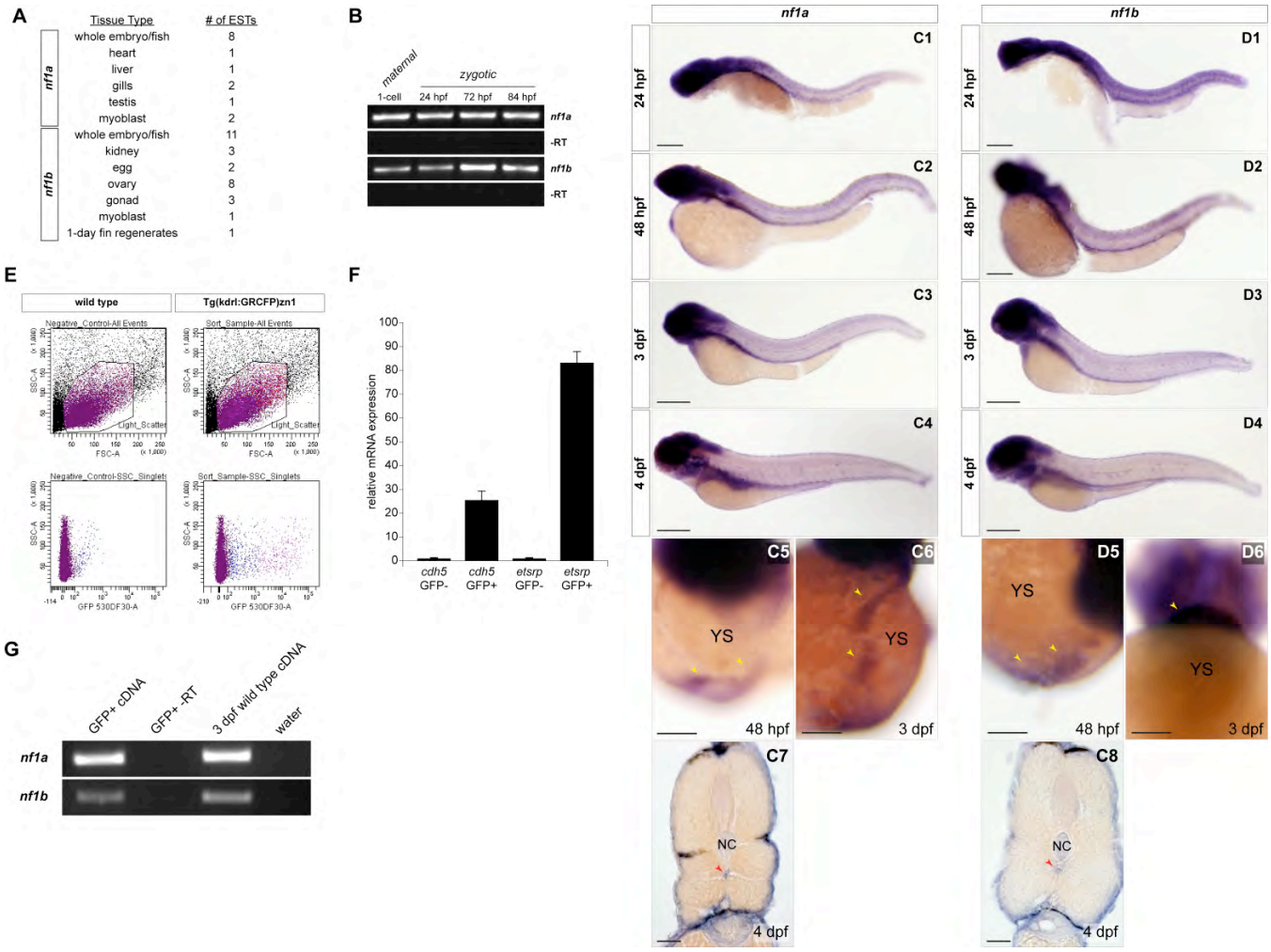

Fig 4. Zebrafish *nf1a* and *nf1b* are expressed during embryonic development.
(**A**) Distribution of ESTs mapping to *nf1a* or *nf1b* in dbEST including tissue of origin. (**B**) RT-PCR analysis verifying maternal (1-cell) and zygotic (24, 72, and 84 hpf) expression of *nf1a* and *nf1b*. (**C1-C6, D1-D6**) Whole-mount *in situ* hybridization of 24 hpf, 48 hpf, 3 dpf (all magnifications of insets in Fig. 3), and 4 dpf zebrafish embryos shows temporal and spatial expression patterns of *nf1a* and *nf1b*. (**C5-6, D5-6**) Both *nf1a* and *nf1b* are expressed in cardiac tissue at 48 hpf and 3 dpf as seen in these anteroventral images. Notably, analysis of 14µm (**C7, D7)** cross sections of whole-mount stained 4 dpf zebrafish embryos reveals strong *nf1a* and *nf1b* expression in the region of the dorsal vessel (arrows) directly below the notochord (NC). **(E)** Parameters utilized for sorting GFP-positive and GFP-negative cells from 3.5 dpf Tg(kdrl:GRCFP)zn1 zebrafish embryos. **(F)** Quantitative PCR analysis of the GFP-positive cell fraction reveals marked enrichment for endothelial-specific genes, including *cdh5* and *etsrp*, relative to the GFP-negative fraction. **(G)** Reverse-transcription and polymerase chain reaction (RT-PCR) for *nf1a* and *nf1b* was performed using first strand cDNA synthesized from endothelial cell RNA (GFP-positive cell fraction), confirming expression of both genes in vascular endothelium. Scale bars: 25µm.

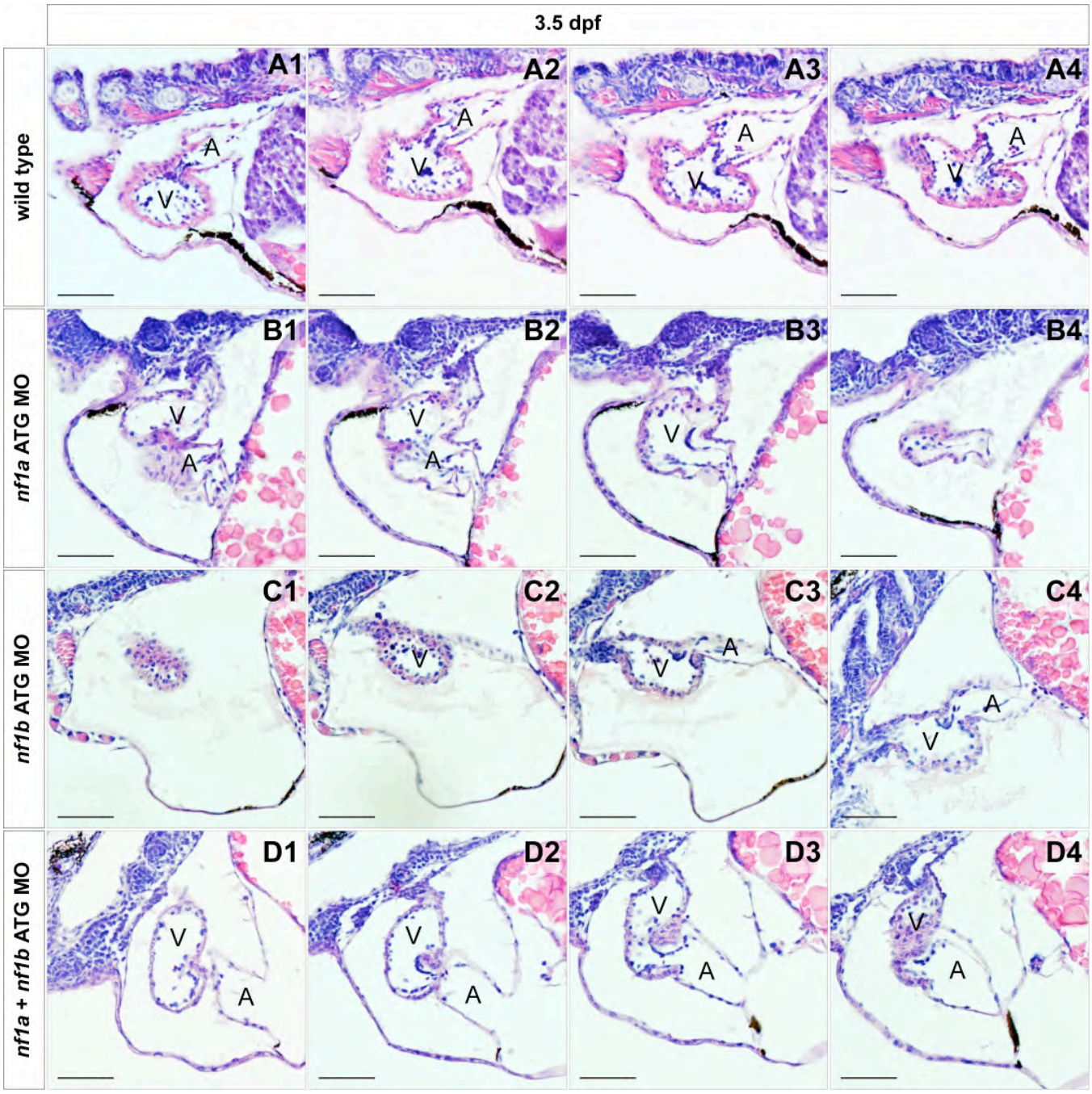

Fig 5. Histological analysis of MO knockdown cardiac valves.
Serial transverse histological sections through the atrio-ventricular valves of wild type **(A1-4)** or ~2ng morphant *nf1a* ATG **(B1-4)**, *nf1b* ATG **(C1-4)**, and *nf1a* + *nf1b* ATG **(D1-4)** 3.5 dpf zebrafish embryos reveal no readily apparent defects at the resolution afforded to us by histological analysis (A, atrium; V, ventricle). Scale bars: 50μm.

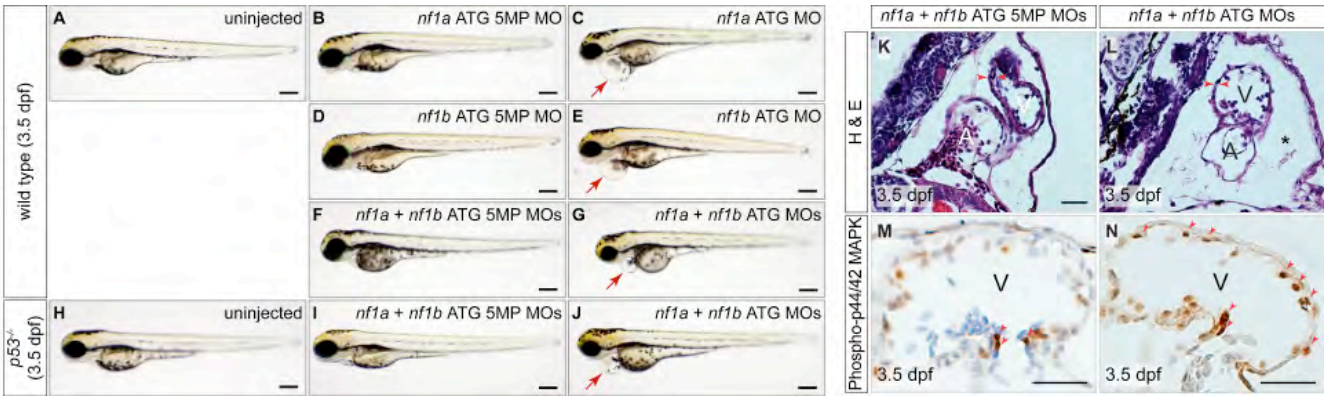

Fig 6. MO knockdown of *nf1a, nf1b,* or both together results in pericardial effusions at 3.5 dpf and increased phospho-p44/42 MAPK in cardiac tissue.
Analysis of 3.5 dpf wild type (**A**), *nf1a* ATG 5-mispair (5MP) MO- (**B**), *nf1b* ATG 5MP MO (**D**), or *nf1a* + *nf1b* ATG 5MP MO- (**F**) injected embryos reveal no apparent defects in gross morphology. Treatment with *nf1a* ATG MO (**C**), *nf1b* ATG MO (**E**), or a combination of both (**G**), however, results in a dilation of the pericardial space. (**H-J**) Injection of $p53^{-/-}$ embryos with *nf1a* + *nf1b* ATG MO results in a gross dilation of the pericardial space (**J**), while uninjected (**H**) and *nf1a* + *nf1b* ATG 5MP MO-injected $p53^{-/-}$ embryos (**I**) appear normal. Scale bars: 0.25mm. (**K-L**) Transverse sections of 3.5 dpf *nf1a/nf1b* combined morphant embryos reveals a thinning of the ventricular myocardium and pericardial effusion (*) when compared with controls (A, atrium; V, ventricle). (**M-N**) Immunohistochemical analysis of transverse sections of 3.5 dpf *nf1a*/*nf1b* combined morphant embryos reveals an increase in the ratio of phospho-p44/42 MAPK positive cardiac cells (arrows) to the total number of cardiac cells when compared to controls. Scale bars: 25μm.

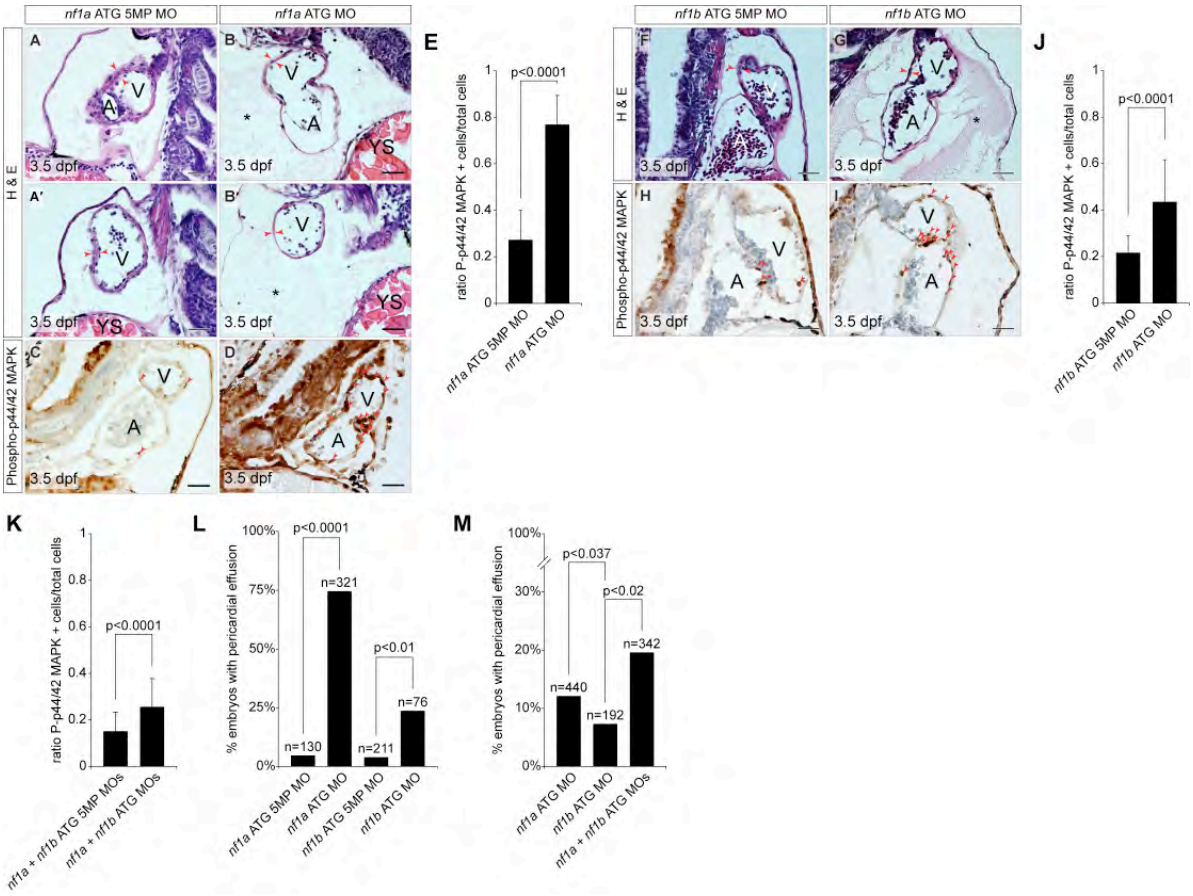

Fig 7. MO knockdown of *nf1a* or *nf1b* results in a thinning of the ventricular myocardium and increased phospho-Erk staining in cardiac tissue.
(**A, A′, B, B′, F, G**) Transverse histological sections through the heart of 3.5 dpf zebrafish embryos reveals a thinning of the ventricular myocardium (red arrows) of zebrafish treated with *nf1a* or *nf1b* ATG MOs when compared with the corresponding controls (A, atrium; V, ventricle; YS, yolk sac). Notably, a large pericardial effusion can be appreciated in *nf1a* and *nf1b* morphants (*). (**C, D, H, I**) Immunohistochemichal analysis of transverse sections through 3.5 dpf zebrafish hearts reveals an upregulation of phospho-p44/42 MAPK (phospho-Erk) in *nf1a* or *nf1b* morphants when compared to the appropriate 5MP controls. The ratio of phospho-Erk positive cardiac cells to the total number of cardiac cells was quantified over multiple sections for *nf1a* MO (2ng), *nf1b* MO (2ng), and *nf1a* + *nf1b* MO (2ng) groups (mean ratio phospho-p44/42 MAPK positive cardiac cells/total cardiac cells ± SD) (**E, J, K**). (**L**) Quantification of percentage of embryos displaying a pericardial effusion phenotype at 3.5 dpf following injection of approximately 2ng of *nf1a* ATG 5MP MO, *nf1a* ATG MO, *nf1b* ATG 5MP MO, or *nf1b* ATG MO. 75% of *nf1a* ATG morphants displayed pericardial effusions as compared to 5% of *nf1a* ATG 5-mispair (5MP) morphant controls ($p<0.0001$). 24% of *nf1b* ATG morphants displayed pericardial effusions as compared to 4% of *nf1b* ATG 5MP morphant controls ($p<0.01$). (**M**) Quantification of percentage of embryos displaying a pericardial effusion phenotype at 3.5 dpf following injection of *nf1a* ATG MO, *nf1b* ATG MO, or *nf1a* + *nf1b* ATG MO. A suboptimal dose (1ng) of *nf1a* ATG MO resulted in a 12% incidence of pericardial effusion, while a suboptimal dose (1ng) of *nf1b* ATG MO resulted in a 7% incidence of pericardial effusion. Injection of 1ng of a combination of *nf1a* + *nf1b* ATG MO, however, resulted in a 20% incidence of pericardial effusion. Scale bars: 25μm.

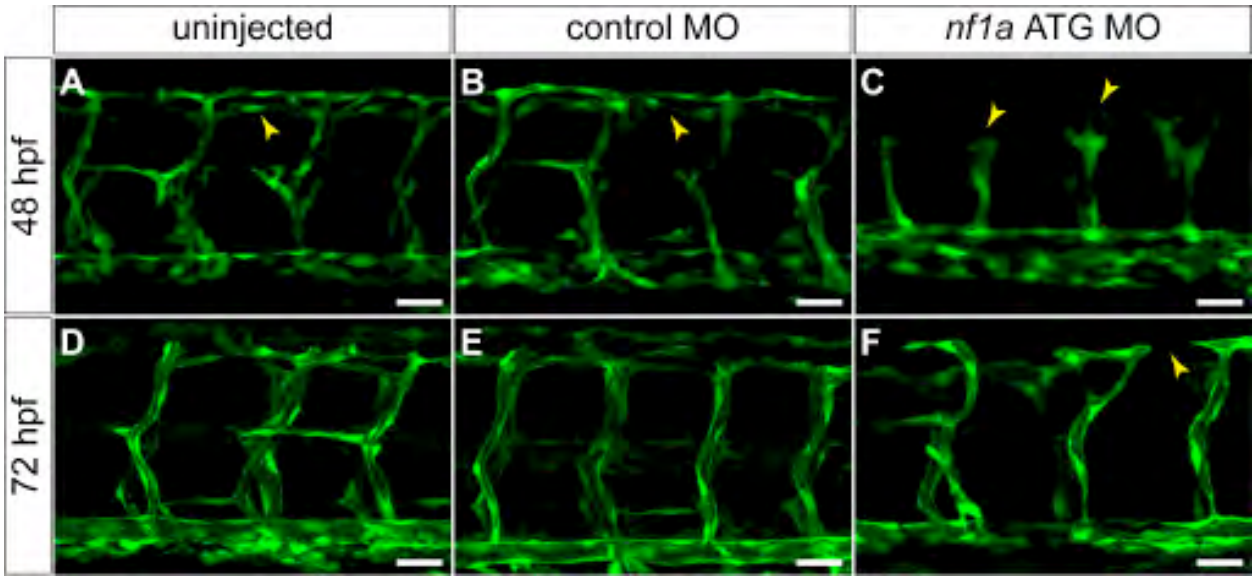

Fig 8. **MO knockdown of *nf1a* results in vascular patterning defects at 48 and 72 hpf.** (**A-C**) At 48 hpf, *nf1a* ATG MO-treated Tg(fli:egfp)y1 (endothelial-specific GFP transgenic) zebrafish embryos display gross defects in vascular development compared with control MO-treated or uninjected samples. Morphant embryos (**C**) display abnormal claw-like projections at the leading edge of the developing intersomitic vessels and fail to develop the dorsal longitudinal anastomotic vessel (DLAV) present in both control MO-treated (**B**) and uninjected (**A**) samples. (**D-F**) At 72 hpf, *nf1a* ATG morphant embryos display only rudimentary DLAVs and a general disorganization of the trunk vasculature (**F**) when compared with control MO-treated (**E**) or uninjected (**D**) embryos. Scale bars: 25μm.

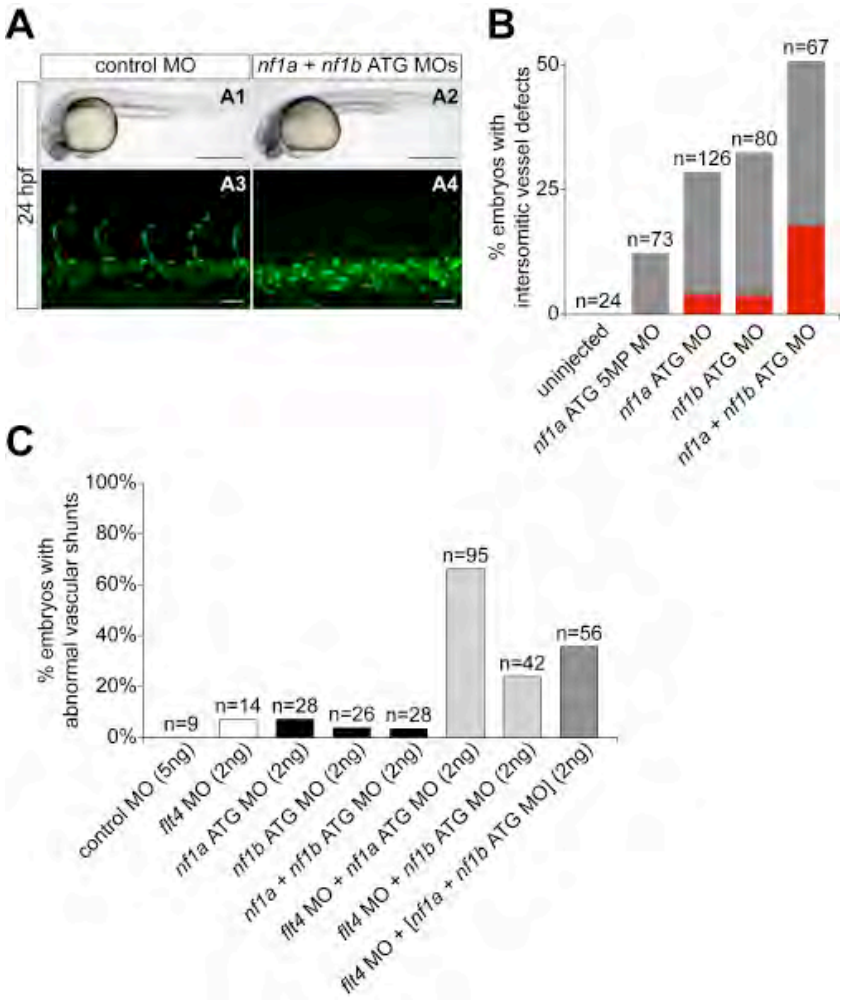

Fig 9. **MO knockdown of *nf1a, nf1b*, or both together result in vascular defects at 24 at 48 hpf.** (**A, B**) Analysis and quantification of vascular defects at 24 hpf in uninjected and morphant Tg(fli:negfp)y7 (endothelial-specific nuclear GFP transgenic) zebrafish embryos. Control MO- (**A1**) and combined *nf1a*/*nf1b* MO-treated (**A2**) zebrafish embryos appear similar by gross morphological analysis at 24 hpf (scale bars: 500μm). Development of intersomitic vessels is deficient at 24 hpf in *nf1a*/*nf1b* combined morphants (**A4**) when compared to controls (**A3**) (scale bars: 25μm). (**B)** Intersomitic vessel formation between somites 17-30 at 24 hpf was scored as absent (red), intermediate (grey), or normal following administration of 2ng of the indicated MO(s). (**C**) MO-mediated knockdown of *flt4*, providing a sensitized background for the detection of vascular defects, was combined with *nf1a, nf1b, and nf1a + nf1b* ATG MO knockdown. 24%-85% of combined *flt4*/(*nf1a*, *nf1b*, *nf1a + nf1b*) MO-treated embryos display abnormal vascular shunts compared with 3-8% of individual *flt4*, *nf1a*, *nf1b*, or *nf1a + nf1b* MO-treated embryos.

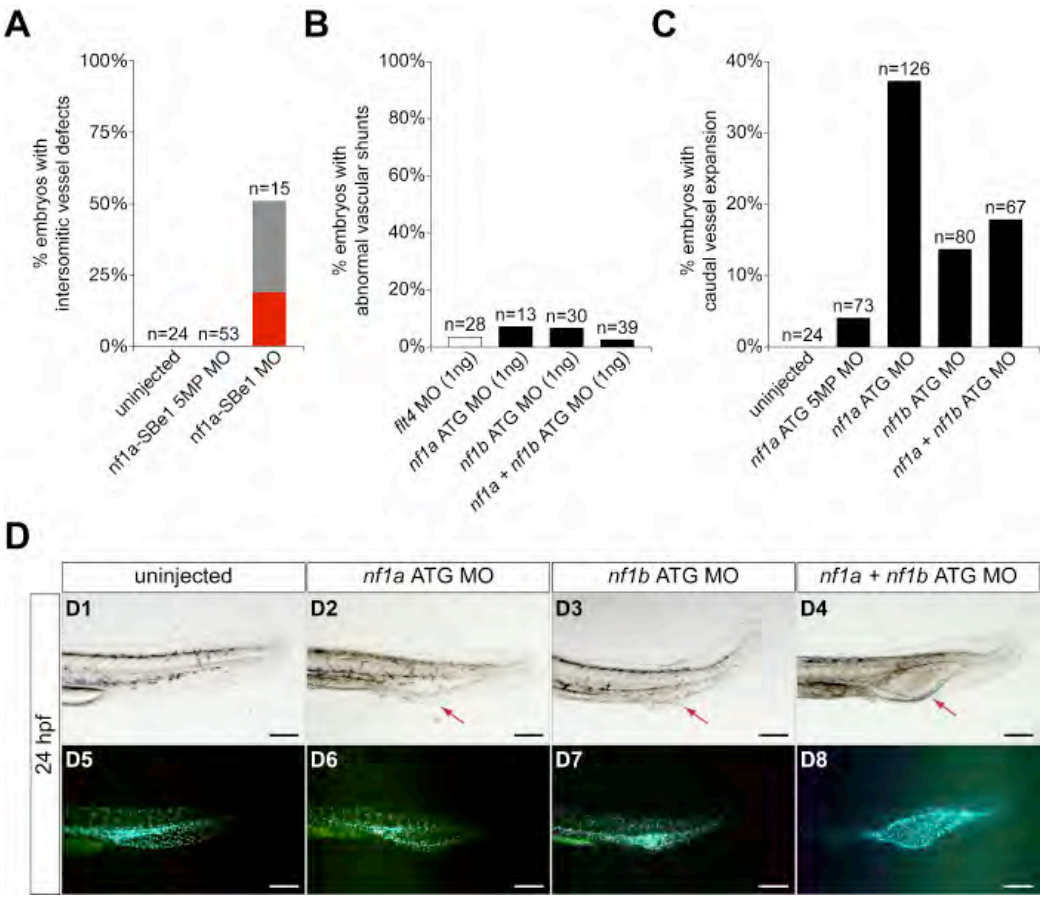

Fig 10. MO knockdown of *nf1a, nf1b,* or both together result in vascular defects at 24 at 48 hpf. (**A**) Quantification of vasculature at 24 hpf in uninjected and morphant Tg(fli:negfp)y7 (endothelial-specific nuclear GFP transgenic) zebrafish embryos. Uninjected, *nf1a*-SBe1 5MP (1ng), and *nf1a*-SBe1 (1ng) morphant embryos were qualitatively assessed for presence, absence (red), or an intermediate phenotype (grey) with regard to the developing trunk intersomitic vessels between somites 17-30 at 24 hpf. (**B**) Quantitation of vascular shunt phenotype seen with low (1ng) doses of *flt4*, *nf1a*, *nf1b*, or *nf1a* + *nf1b* MOs. (**C**) Quantitation of cystic expansion phenotype observed in morphant Tg(fli:negfp)y7 embryos treated with 2ng of the indicated MO(s). (**D1-D8**) Treatment of Tg(fli:negfp)y7 zebrafish embryos with an *nf1a* ATG MO, *nf1b* ATG MO, or *nf1a* + *nf1b* ATG MOs leads to a cystic expansion in the region of the caudal artery and vein (arrows, D2-D4) not present in uninjected embryos (**D1**). The expanded tissue was confirmed to be vascular by GFP expression (**D6-D8**). Scale bars: 50μm.

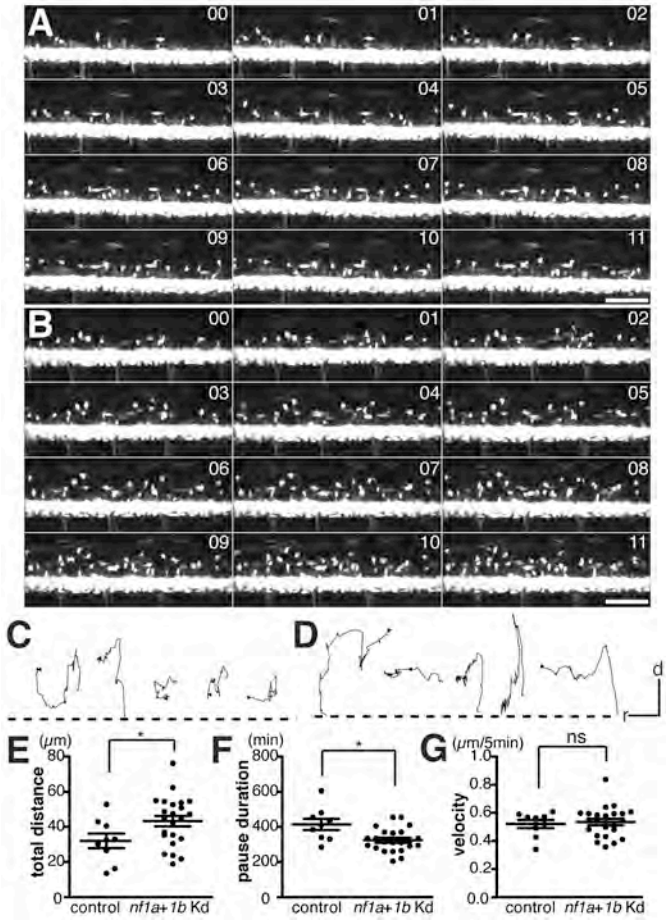

Fig 11. *nf1* loss affects the migration of OPCs.
(**A, C**) An uninjected *olig2-EGFP*; *p53 e7/e7* control embryo; (**B, D**) An *olig2-EGFP*; *p53 e7/e7* embryo injected with *nf1a+1b* morpholinos. (**A, B**) Montages of 12-hour time-lapse images from 60 hpf to 72 hpf, showing the movements of OPCs every hour. Numbers in each panel denote the hour(s) after the start of imaging. For the complete movies, refer to Movie S1, S2. (**C, D**) Cell migration paths are shown for five OPCs that traveled the farthest during the observation period. In both conditions, migration patterns are highly dynamic. Arrowheads indicate the end point of the cell's migration. The dashed lines represent the dorsal-most GFP^+ domains of the ventral spinal cord. Top, dorsal (d); left, rostral (r). (**E**) Graph showing the total distance OPCs travel with or without *nf1* loss. (**F**) Graph showing the total time individual OPCs spent pausing. (**G**) Graph showing the velocity of OPCs calculated from when they were actively migrating. All individual OPCs (represented by single points) that could be observed in the field of view throughout the entire period, spanning the 12-hour imaging period, were traced and used in this analysis (n=9 for uninjected control embryos, n=23 for *nf1a+1b* morphant embryos). The data in E-G are reported as mean ± SEM; asterisks indicate nonparametric statistical significance (∗ < 0.05; ns, not significant). Scale bars in A, B = 25 μm, C, D, the X axis = 10μm and the Y axis = 5 μm.

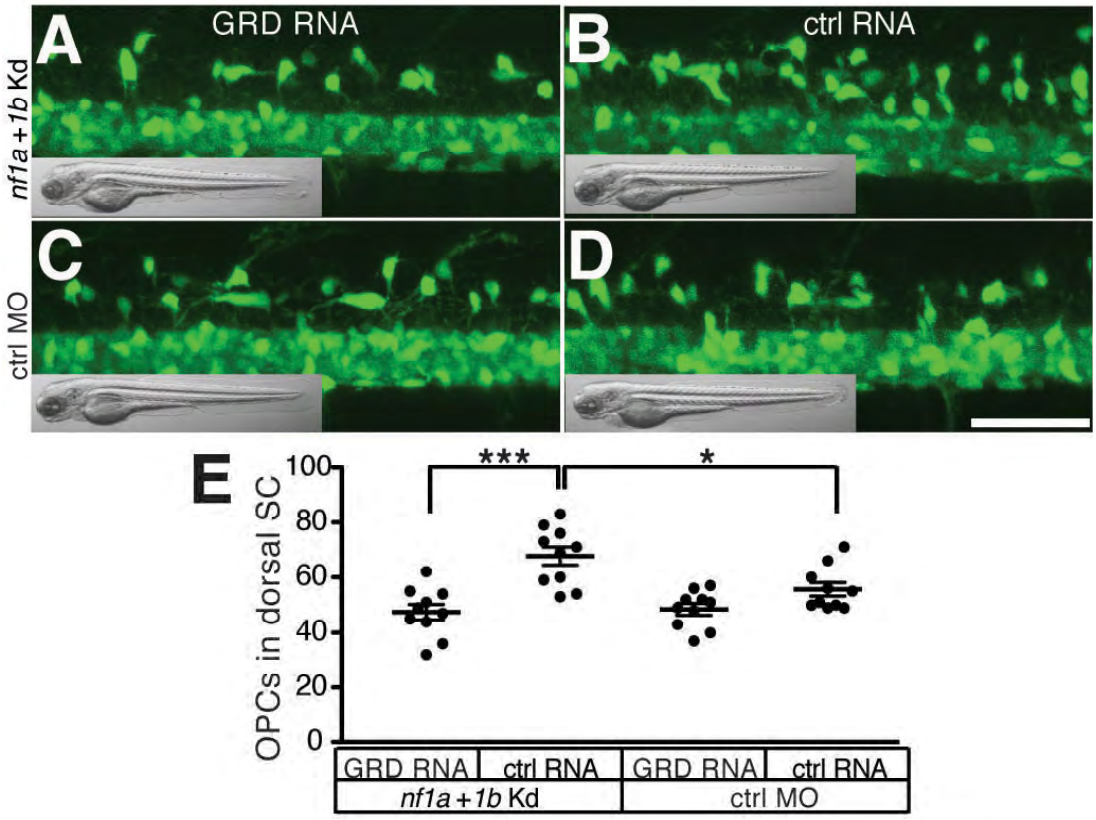

Fig 12. Forced expression of the GRD of *NF1* is sufficient to rescue the aberrant phenotype.
(**A**-**D**) Projected confocal images showing the lateral view of the spinal cord of *olig2-EGFP*; *p53 e7/e7* embryo at 3dpf: *A*, *B*, *nf1a+1b* morpholino; **C**, **D**, control morpholino; **A**, **C**, GRD RNA-injected; **B**, **D**, mCherryRed (control) RNA-injected. Insets show the bright field images of the embryos used for confocal imaging and demonstrate normal overall morphologies in all cases. Scale bar = 50 μm. (**E**) Graph showing the number of OPCs, represented by individual points, in the dorsal spinal cord (SC) of 10 embryos for each condition at 3 dpf. (∗ < 0.05; ∗∗∗ < 0.001). The data is presented as means ± SEM.

A

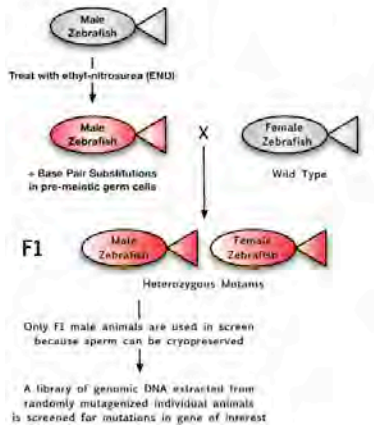

B

Nf1a	exon	mutation	Amino acid change
1 (M82)	Exon21	A**C**G→A**T**G	Thr→Met
2 (F211)	Exon21	C**C**G→C**T**G	Pro→Lys
3 (dir. seq.)	Exon26	CA**G**→CA**C**	Gln→His
4 (74-11)	Exon26	**T**CA→**C**CA	Ser→Pro
5 (VU180)	Exon26	A**T**G→A**A**G	Met→Lys
6 (T203)	Exon26	T**T**G→T**A**G	Leu→stop
Nf1b	**exon**	**mutation**	**Amino acid change**
zm-00346420	intron between Exon1 and Exon2	insertion	N/A

Fig. 13. Searching for zebrafish mutants for *nf1a* and *nf1b*
(A) Schematic of TILLING procedure. **(B)** A list of the mutations for *nf1a* and *nf1b* identified from TILLING thus far.

Fig. 14. ZFN-induced *nf1a* and *nf1b* stable mutant zebrafish lines
Schematic representation of the *nf1a* and *nf1b* mutant alleles generated using ZFN technology.

	$nf1a^{ZFN\_mut2}$; $nf1b^{ZFN\_mut2}$	$nf1a^{ZFN\_mut1}$; $nf1b^{ZFN\_mut3}$	$nf1a^{T203}$; $nf1b^{ZFN\_mut2}$	**marked cell types**
Tg(olig2:egfp)	O	O	O	OPCs and oligodendrocytes (CNS)
Tg(sox10:egfp)	O	O	X	OPCs and oligodendrocytes (CNS), Schwann cells (PNS)
Tg(nkx2.2a:mgfp)	O	O	X	developing myelin (CNS), perineurial glia (PNS)
Tg(3.9nestin:gfp)	O	X	X	neural precursor (CNS)
Tg(brn3c:gfp)	O	X	X	optic nerve
Tg(dbh:gfp)	O	X	X	sympathetic ganglion
Tg(kdrl:grcfp)	O	O	X	endothelial cells
Tg(fli:negfp)	O	O	X	endothelial cells (nuclear)
Tg(c236:GFP)	X	X	X	developing AV valve

Table 1. Three *nf1a;nf1b* double mutant alleles crossed with transgenic lines (O= line is generated; X= line is being established.)

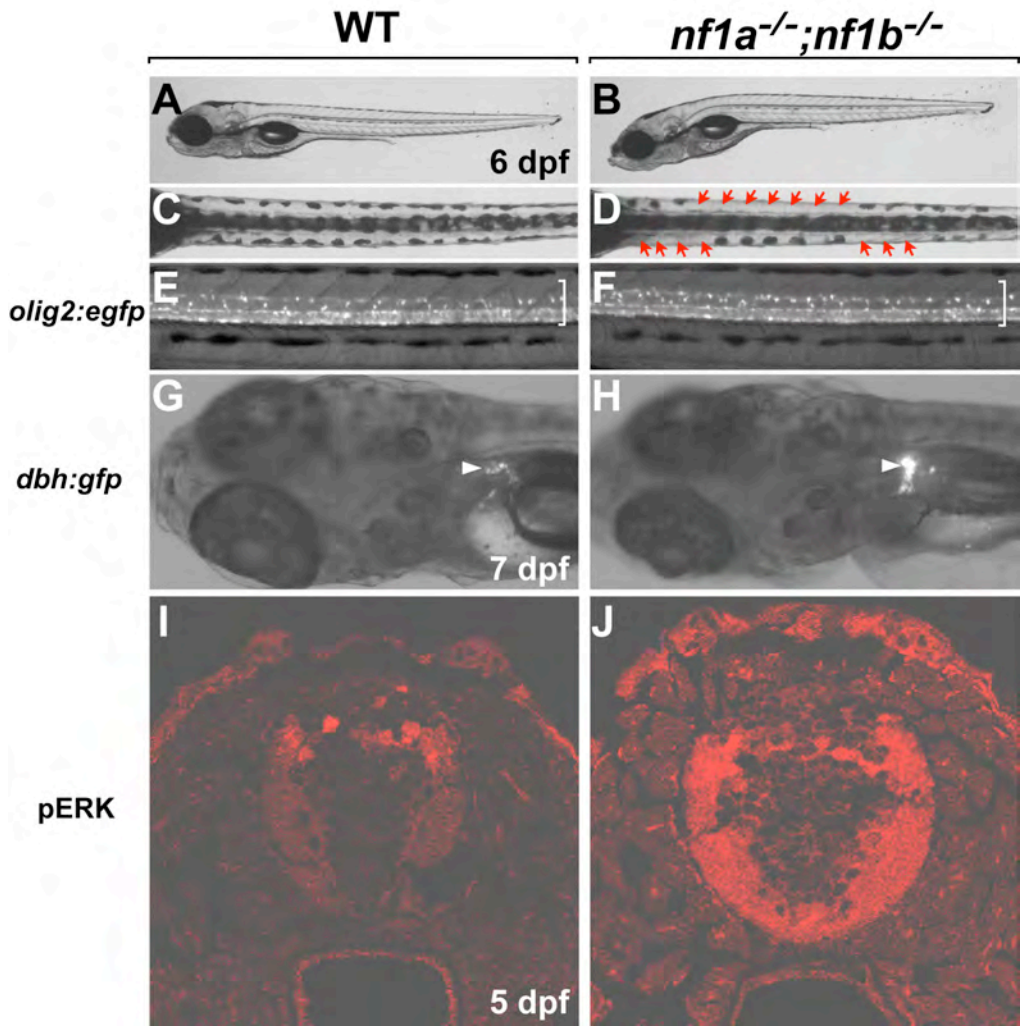

Fig 15. Phenotypes of *nf1a;nf1b* double mutant.
(**A,C,E,G,I**) Wild-type. (**B,D,F,H,J**) *nf1a*$^{ZFN\_mut2}$;*nf1b*$^{ZFN\_mut2}$ double homozygous mutant. (A-D) Brightfield images. (E-H) Epi-fluorescent images. (I,J) Confocal images. (A,B) Overall morphology of the mutant looks normal at 6 dpf. (C,D) Dorsal view of the tail region. Arrows indicate missing melanocytes in the lateral strip of the mutant. (E,F) *nf1a;nf1b* mutant larva has more dorsally migrated *olig2:*EGFP^{+} OPCs than control (bracket). (G,F) At 7 dpf, *dbh:*GFP^{+} SCG (arrowhead) is enlarged in the mutant larva. (I,J) Transverse sections, dorsal up. Phospho-ERK1/2 is highly detected in a few neurons and white matter of the spinal cord of the *nf1a;nf1b* mutant larva.